RSC Advances

PAPER

View Article Online
View Journal | View Issue

Cite this: *RSC Adv.*, 2017, 7, 10692

Highly stable and biocompatible $W_{18}O_{49}$@PEG-PCL hybrid nanospheres combining CT imaging and cancer photothermal therapy

Jianning Mu,†[a] Xiaoyu Meng,†[b] Li Chen,†[c] Zhanbin Lu,[a] Qinwei Mou,[d] Xiaoxue Li,[e] Suiqin Wang†*[f] and Hongyun Yue†*[f]

Received 13th December 2016
Accepted 31st January 2017

DOI: 10.1039/c6ra28161c

rsc.li/rsc-advances

In this study, we encapsulated $W_{18}O_{49}$ NPs with PEG-PCL NPs ($W_{18}O_{49}$@PEG-PCL NPs). The PEG-PCL NPs enhance the biocompatibility, stability and internalization of the $W_{18}O_{49}$ NPs in cells. Retained for a long time, these $W_{18}O_{49}$@PEG-PCL NPs possess excellent CT efficiency and superior PTT potency, which confer them with the potential to play an active role in future clinical trials.

Introduction

Many heavy metals such as gold,[1–4] platinum,[5] bismuth,[6] silver,[7] tantalum,[8] tungsten,[9–13] and rare earth metals[14,15] have been extensively studied as computed tomography (CT) contrast agents in an effort to replace the traditional iodine enhanced CT contrast agent, which generally requires a large injection dose and causes strong side effects. Recently, tungsten oxide nanoparticles (TONPs) were employed for CT imaging and photothermal therapy (PTT) due to their high X-ray attenuating potency and strong localized surface plasmon resonance (LSPR) properties.[16] Afterwards, Hu *et al.* synthesized ultrafine $W_{18}O_{49}$ NPs *via* a polyol method, which exhibited excellent water dispersity.[9] Compared with traditional PTT candidates (*e.g.*, Au nanorods), $W_{18}O_{49}$ NPs possess several advantages described as follows: (1) higher cost effectiveness and facile synthesis procedures that can be easily scaled up; (2) optimal size for lymphatic imaging (<10 nm) with respect to previously reported materials;[17] (3) the PTT of the NPs can be rendered *via* irradiation with a 1064 nm laser. The wavelength of the 1064 nm laser is long enough for deep skin penetration and high body tolerance.[18] Unfortunately, once exposed to air, $W_{18}O_{49}$ NPs are quickly oxidized into various ions without strong LSPR properties. Furthermore, for renal failure patients, the *in vivo* formation of high osmotic pressure due to the ionic CT contrast agent can cause some adverse reactions.[19] Hence, there is a great need to fabricate $W_{18}O_{49}$ NPs with excellent stability and water dispersibility, to be used as a CT agent and PTT agent in the clinic. Unfortunately, there has been little work related to the fabrication of $W_{18}O_{49}$ NPs.

In this study, we synthesized $W_{18}O_{49}$@PEG-PCL NPs, which not only have the advantages of $W_{18}O_{49}$ NPs, but also exhibit longer lasting stability. Furthermore, five cycles of NIR laser irradiation was performed on the $W_{18}O_{49}$@PEG-PCL NPs and Au nanorods (the most common PTT agent), respectively. Compared with the Au nanorods, the $W_{18}O_{49}$@PEG-PCL NPs exhibited better photothermal conversion stability. Tumor tissue has a vascular system containing pores with sizes in the range of 20–500 nm, giving rise to a phenomenon known as the enhanced permeability and retention effect (EPR).[20–22] *In vitro* cellular uptake tests demonstrated that equipping $W_{18}O_{49}$ with PEG-PCL can take advantage of EPR to implement the passive enrichment of NPs in the tumor location. An *in vitro* CT study and a cytotoxic assay revealed that $W_{18}O_{49}$@PEG-PCL NPs exhibit an excellent CT imaging effect, good biocompatibility and are suitable for *in vivo* applications. Eventually, the superior PTT potency of $W_{18}O_{49}$@PEG-PCL NPs will lead to their potential usage in the treatment of cancer.

Experimental section

Materials

mPEG-OH (M_w: 5000 Da) was purchased from Beijing JenKem Technology Company. *N*,*N*-dimethylformamide (DMF) was purified by dehydration over CaH_2 at room temperature and distilled under reduced pressure. ε-Caprolactone (ε-CL), tungsten hexachloride (WCl_6), diethylene glycol (DEG), poly acrylic acid (PAA, M_w = 1800 Da), ethyl dimethylaminopropylcarbodiimide (EDC) and *N*-hydroxysulfosuccinimide sodium salt (sulfo-NHS) were all purchased from Sigma-Aldrich. All

[a]*Department of Gynaecology, Xi'an Gaoxin Hospital, Xi'an 710000, China*
[b]*Department of Gynaecology and Obstetrics, Yulin Second Hospital of Shaanxi Province, Yulin 719000, China*
[c]*Department of Gynaecology, Baoji City Hospital Maternity and Child Health Care Hospital, Baoji 721000, China*
[d]*Obstetrical Department, Shaanxi Baoji Maternal and Child Health Hospital, Baoji 721000, China*
[e]*Department of Gynaecology and Obstetrics, Ankang City Central Hospital, Ankang 725000, China*
[f]*Obstetrical Department, Yanan University Affiliated Hospital, Yanan 716000, China. E-mail: yuehong-yun1976@126.com; wangsuiqin1971a@163.com*
† These authors contributed equally to this work.

other chemicals were purchased from J&K Chemicals and used as received without further treatment. Human ovarian cancer (HeLa) cells were obtained from Fudan University (Shanghai, China).

Synthesis of $W_{18}O_{49}$

Based on a previous study, $W_{18}O_{49}$ NPs can be synthesized by reducing WCl_6 with alcohol.[23] Here, we used diethylene glycol (DEG) as the solvent, because it is suitable for high temperature reactions. Briefly, WCl_6 (800 mg) and PAA (200 mg) were dissolved in DEG (50 mL), and the suspension was heated at 160 °C for 10 min and was then allowed to cool down to room temperature. Then deionized water (50 mL) was added into the mixture to induce precipitation. The as-obtained $W_{18}O_{49}$ NPs were collected by centrifugation and washed thoroughly with deionized water five times to remove the residue. $W_{18}O_{49}$ NPs (510 mg) were obtained after lyophilisation.

Synthesis of PEG-PCL

ε-CL was mixed with a certain amount of m-PEG-OH, and the mixture was stirred at 160 °C for 24 h in a vacuum-sealed tube. After the polymerization was completed, the crude copolymers were dissolved in DCM and precipitated in an excess amount of cold ethyl ether to remove the unreacted monomer and oligomer. The precipitates were then filtered and dried under reduced pressure.

Synthesis of $W_{18}O_{49}$@PEG-PCL

PEG-PCL (50 mg) was suspended in deionized water (50 mL). After 5 min of ultra-sonication, dichloromethane suspension (5 mL) containing $W_{18}O_{49}$ (10 mg) was added into the above-mentioned suspension. The mixture was allowed to react for another 30 min of ultra-sonication. The as-obtained $W_{18}O_{49}$@PEG-PCL NPs were collected by centrifugation and washed thoroughly with deionized water five times to remove the residue.

Characterization

^{1}HNMR was carried out using a Bruker AV400 spectrometer with tetramethylsilane as an internal standard and $CDCl_3$ as the solvent. The morphologies of the as-synthesized $W_{18}O_{49}$, PEG-PCL, and $W_{18}O_{49}$@PEG-PCL NPs were investigated by transmission electron microscopy (TEM, JEOL TEM-100) and high resolution TEM (JEOL, TEM-2100). The UV-vis absorption spectra of the as-synthesized $W_{18}O_{49}$, PEG-PCL, and $W_{18}O_{49}$@PEG-PCL NPs were recorded on a spectrophotometer (UV3100, Shimadzu, Japan). The size distribution and zeta potentials were determined using a dynamic light scattering (DLS) method (BI-9000AT, Brookhaven, USA). Thermogravimetric analyses (TGA) were performed using a TAC71DX thermal analyser under air flow in the temperature range 25–800 °C at a heating rate of 20 °C min^{-1}. The tungsten concentrations were quantified using inductively coupled plasma-mass spectrometry (ICP-MS, PerkinElmer Corporation, USA). Digestion of the samples was performed in concentrated nitric acid and the samples were heated at 90 °C for 12 h before the measurements. All results were taken as the average of triplicate measurements. In the study of the photothermal effect, a 1064 nm diode laser (LEO photonics Co. Ltd) and an 808 nm diode laser (LE-LS-808-3000TFC-D, Leo Photonics Company, Shanghai) were employed, with the output power tunable from 0 to 10 W cm^{-2}. The temperature increment under laser irradiation was determined in a quartz cell with a tinfoil cap to prevent the vaporization of water. The final photothermal conversion efficiency (η) was calculated using the following equation:

$$\eta\ (\%) = \frac{cm\Delta t}{wt} \times 100\% = \frac{4.2 \times 10^3 \times 1 \times 10^{-3}\Delta t}{0.5 \times 600} \times 100\%$$

In vitro cellular uptake

In vitro cellular uptake studies of the $W_{18}O_{49}$ NPs and $W_{18}O_{49}$@PEG-PCL NPs by HeLa cells were conducted using fluorescent microscopy. HeLa cells were seeded in 35 mm petri dishes. After 24 h incubation, $W_{18}O_{49}$ NPs and $W_{18}O_{49}$@PEG-PCL NPs (conjugated with Cy5.5) at a concentration of 1 mg mL^{-1} were then separately introduced into the system for 2 h. The medium was then discarded, and the cells were washed with PBS three times. After that, the cell nuclei and f-actin were stained with 4′,6-diamidino-2-phenylindole (DAPI) and fluorescein isothiocyanate (FITC) labeled phalloidine according to the manufacturer's instructions, respectively. Finally, the cells were fixed with 4% paraformaldehyde and observed using a fluorescence microscope (Carl Zeiss, Germany) equipped with an optiMOS CCD (Qimaging). Acquired fluorescence images were further merged using ImageJ software.

In vitro X-ray attenuation study (CT experiments)

Suspensions containing equivalent concentrations of $W_{18}O_{49}$ NPs, $W_{18}O_{49}$@PEG-PCL and the clinical iodine contrast agent iodixanol (with respect to tungsten and iodine concentration: 6.25, 12.5, 25, 50, 100 mM) were added into a 48-well cell culture plate. CT images were collected using a clinical CT Gemstone spectral 64-Detector CT (Discovery CT 750HD, GE Amersham Healthcare System, Milwaukee, WI), and the images were acquired at an X-ray voltage of 65 kVp and an anode current of 500 μA.

In vitro cytotoxicity assay (MTT assay)

The cytotoxicity of the $W_{18}O_{49}$@PEG-PCL NPs was detected *via* a MTT (3-(4,5-dimethylthiazol-2-yl)-2,5-diphenyltetrazolium bromide) assay. Briefly, HeLa cells were seeded in 96-well plates at a density of 10^4 cells per well in 100 mL of Iscoves modified Dulbecco's medium and were incubated overnight at 37 °C in a 5% CO_2 atmosphere. The medium of each well was replaced with 100 mL fresh medium containing various concentrations of the $W_{18}O_{49}$@PEG-PCL NPs. All concentrations were tested in five replicates. After 24 h incubation (and then laser exposure at an energy density of 0.5 W cm^{-2} for 4 min or not) and 48 h incubation, the medium was aspirated, and the cells were washed twice with phosphate-buffered saline (PBS, pH 7.0), followed by the addition of 20 mL of MTT solution (2.5 mg mL^{-1} in PBS). The cells were then incubated for another 4 h at 37 °C. After that, the medium was aspirated. The collected cells were resuspended in 200 mL DMSO, and the absorbance of each well at 490 nm was measured using an iMark Enzyme mark instrument (BIO-RAD Inc., USA).

In vitro PTT capability verified *via* live/dead double staining method

For *in vitro* PTT, HeLa cells were cultured with $W_{18}O_{49}$@PEG-PCL NPs (1 mg mL^{-1}). After 4 h incubation, the media were discarded and the cells were subjected to laser irradiation (1064 nm, 0.5 W cm^{-2}) for 4 min after three washes with PBS suspension. To determine the viability of the cells post treatment, the cells were labeled with calcein AM and PI (Live/Dead Kit, Invitrogen) according to the manufacturer's instructions. Then, the cells were imaged directly with laser scanning confocal microscopy (LSCM) without formalin fixation.

Results and discussion

Characterization of $W_{18}O_{49}$ NPs and PEG-PCL

XRD analysis (Fig. 1A) confirmed that these as-synthesized nanoparticles were $W_{18}O_{49}$ NPs, and the peaks could be well indexed to the monoclinic phase (JCPDS no. 712450). Detailed investigation of peaks corresponding to tungsten revealed the mixed bonding state manner (Fig. 1B, W^{5+} and W^{6+}) of the tungsten element in the $W_{18}O_{49}$ NPs, in agreement with the results reported by Sato and co-workers.[27] Fig. 1C shows the ^{1}H NMR spectra of PEG-PCL, which demonstrates the four major characteristic peaks of PCL at 1.62 (c), 1.40 (d), 2.31 (b) and 3.65 (e) ppm, attributed to the repeating units of PCL. The peak at about 4.07 (a) ppm is related to PEG, and based on the ^{1}H NMR data, PEG-PCL was successfully synthesized.

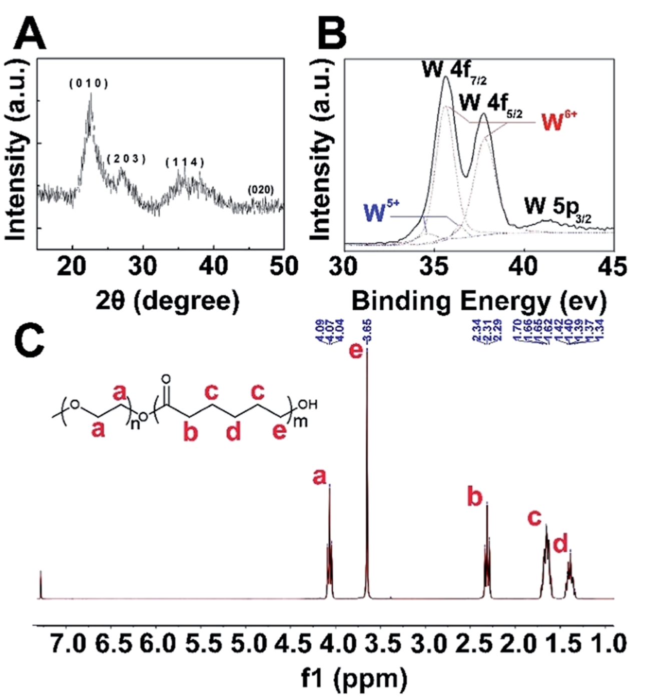

Fig. 1 (A) XRD pattern of the $W_{18}O_{49}$ NPs. (B) Representative X-ray photoelectron spectroscopy results of the $W_{18}O_{49}$ NPs and the corresponding peak of the tungsten element. (C) ^{1}H NMR spectrum of PEG-PCL.

Preparation and characterization of $W_{18}O_{49}$@PEG-PCL NPs

Fig. 2 schematically shows the preparation of the $W_{18}O_{49}$@PEG-PCL NPs. PEG is soluble in water, while PCL and $W_{18}O_{49}$ are soluble in dichloromethane. The $W_{18}O_{49}$@PEG-PCL NPs were synthesized *via* self-assembly. Homogeneously dispersed $W_{18}O_{49}$ NPs are clearly shown in the transmission electron microscopy (TEM) image in Fig. 3A. The addition of PAA would modify $W_{18}O_{49}$ with carboxyl groups. The ionization of carboxylic acid groups would cause repulsion among the anions of carboxylic acid (COO^-) and prevent the aggregation of the NPs, which contributes to the homogeneous size and shape. A lattice spacing equalling 0.38 nm (Fig. 3A, inset) was distinctly observed using high resolution TEM (HRTEM), which corresponded to the (010) lattice plane of the $W_{18}O_{49}$ NPs. These $W_{18}O_{49}$ NPs had a narrow size distribution with an average size of 6.7 nm (Fig. 3A), which is smaller than the value (16.8 nm) obtained from the dynamic laser scattering (DLS) results (Fig. 3C). After encapsulation of $W_{18}O_{49}$ NPs in the PEG-PCL NPs, uniformly spherical and mono-dispersed NPs can be seen in the TEM image (Fig. 3B) with an average diameter of 108 nm, which is smaller than the hydrodynamic diameter (152 nm, Fig. 3D). The fine structure of the $W_{18}O_{49}$@PEG-PCL NPs is further demonstrated in the HRTEM image (Fig. 3B, inset) with a remarkable variation in the contrast between the light shell and dark core. The presence of the dark core confirms that a large number of $W_{18}O_{49}$ NPs were successfully wrapped in PEG-PCL shells, owing to the high electron density of the $W_{18}O_{49}$ NPs. By a close observation, small dark dots with sizes of less than 10 nm are clearly observed in the core, which also confirms the presence of $W_{18}O_{49}$ NPs. In addition, the $W_{18}O_{49}$ encapsulation content and encapsulation efficiency are 15.2% and 84.2% for $W_{18}O_{49}$@PEG-PCL NPs, respectively, based on the TGA analysis as shown in Table 1.

Optical properties of the hybrid NPs

From the UV-vis spectra shown in Fig. 4A, the PEG-PCL NPs have no absorption in the NIR region, while for the $W_{18}O_{49}$ NPs, a gradual increase in the absorption intensity as a function of wavelength up to the NIR region can be seen in the UV spectrum. After encapsulation of $W_{18}O_{49}$, the appearance of the absorption curve of $W_{18}O_{49}$@PEG-PCL NPs is not much different compared to that of naked $W_{18}O_{49}$, which means that the covering layer of PEG-PCL doesn't hamper the LSPR features of the NPs. As the carrier of CT and PTT agents ($W_{18}O_{49}$), the PEG-PCL NPs play a significant role in the long-term stability of $W_{18}O_{49}$. For example, the $W_{18}O_{49}$ NPs are difficult to keep stable in water without the isolation of oxygen. However, after encapsulation, PEG-PCL NPs protect the $W_{18}O_{49}$ NPs well from hydrolysis and oxidation in aqueous solution. From the UV-vis spectra of the naked $W_{18}O_{49}$ NPs (Fig. 4B) and $W_{18}O_{49}$@PEG-

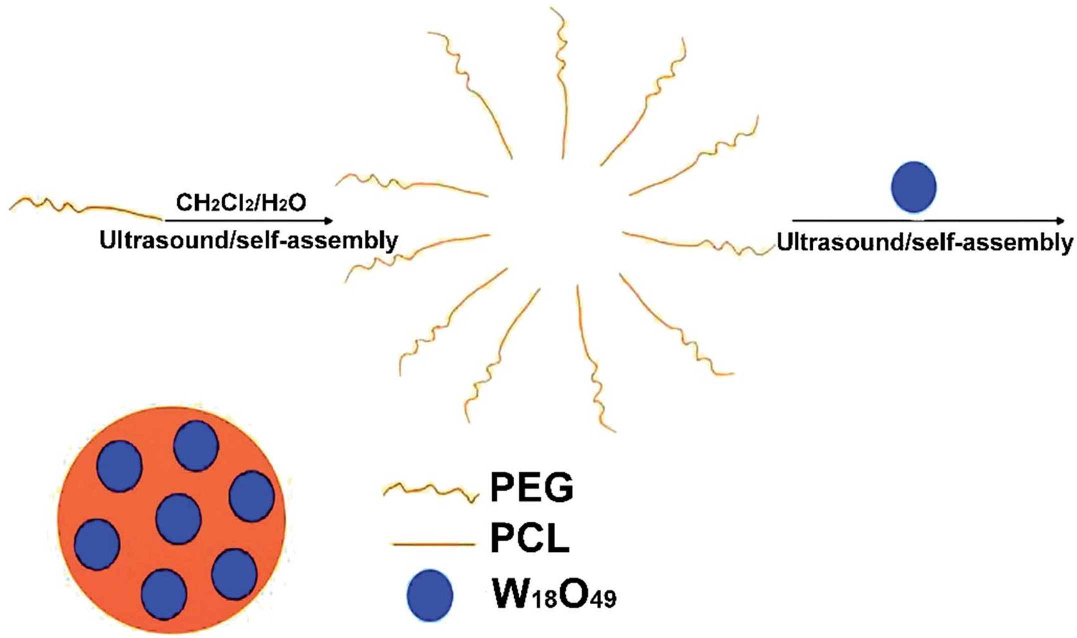

Fig. 2 Synthesis of the $W_{18}O_{49}$@PEG-PCL NPs.

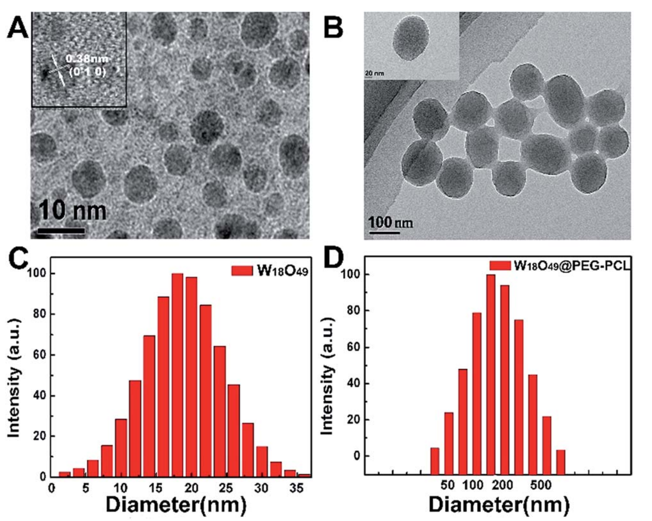

Fig. 3 (A) HRTEM images of the $W_{18}O_{49}$ NPs (inset: lattice space); (B) TEM images of the $W_{18}O_{49}$@PEG-PCL NPs (inset: HRTEM of $W_{18}O_{49}$@PEG-PCL NPs); (C) DLS of the $W_{18}O_{49}$ NPs; (D) DLS of the $W_{18}O_{49}$@PEG-PCL NPs.

Table 1 The thermal weight data for the PEG-PCL NPs and $W_{18}O_{49}$@PEG-PCL NPs

	Proportion of weight (%)			
	100–700 °C	Above 700 °C	Encapsulation content (%)	Encapsulation content (%)
PEG-PCL	68.9	24.1	15.2	84.2
$W_{18}O_{49}$@PEG-PCL	54.4	38.0		

PCL NPs (Fig. 4C), after storing in aqueous solution for three weeks at room temperature, we can see that the spectrum of the naked $W_{18}O_{49}$ NPs is notably changed after storing for just one week, compared to that of the fresh $W_{18}O_{49}$ NPs, implying that the $W_{18}O_{49}$ NPs are unstable in aqueous medium, and oxidation occurs.

In contrast, the spectra of the $W_{18}O_{49}$@PEG-PCL NPs show little change after they are stored in aqueous solution for even three weeks. The optical properties of $W_{18}O_{49}$ encapsulated by PEG-PCL NPs can be retained over a period of three weeks. Apparently, the protection provided by the PEG-PCL NPs is sufficient to prevent degradation of $W_{18}O_{49}$ in aqueous solution. The $W_{18}O_{49}$@PEG-PCL NPs are effective photothermal agents that can produce faster and higher heat effects in terms of photothermal efficiency under irradiation, owing to the gradual increase in absorption intensity as a function of wavelength up to the NIR region (as seen in the UV spectrum of the $W_{18}O_{49}$@PEG-PCL NPs). NIR irradiation (in our manuscript a 1064 nm diode laser was employed) matches the high absorption intensity of our NPs (phototherapeutic window). Furthermore, NIR irradiation possesses deeper tissue penetration and could be applied to irradiate deeper *in vivo* tumors.

Photothermal effects of the $W_{18}O_{49}$ NPs and $W_{18}O_{49}$@PEG-PCL NPs

From Fig. 5A and B, we can conclude that photothermal efficiency increased with the increase in the power density of the 1064 nm laser and the concentration of the $W_{18}O_{49}$@PEG-PCL NPs. The temperature of aqueous dispersions of $W_{18}O_{49}$@PEG-PCL NPs reached 64.2 °C (control in Fig. 5D) after irradiation for 300 seconds at a concentration of 1 mg mL^{-1} under a 0.5 W cm^{-2} 1064 nm laser, which is sufficient for cancer cell

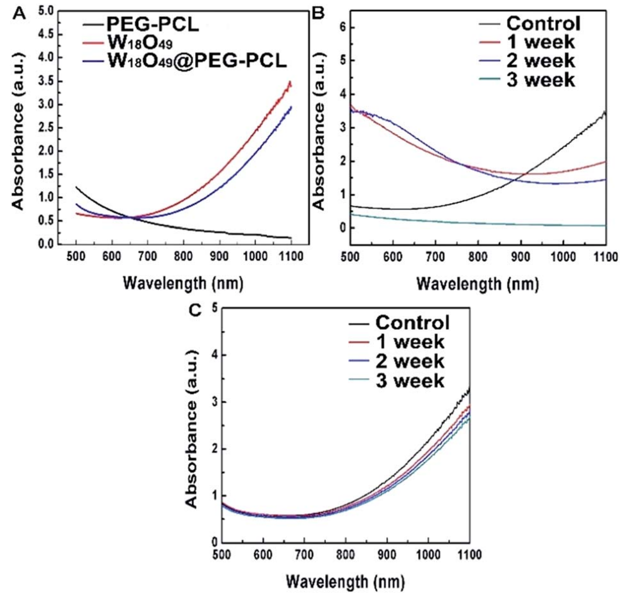

Fig. 4 (A) UV-vis spectra of $W_{18}O_{49}$ NPs, PEG-PCL NPs and $W_{18}O_{49}$@PEG-PCL NPs. (B) UV-vis spectra of naked $W_{18}O_{49}$ NPs after storing in aqueous solution for three weeks at room temperature. (C) UV-vis spectra of $W_{18}O_{49}$@PEG-PCL NPs after storing in aqueous solution for three weeks at room temperature.

killing. The same behaviour of temperature rise for the $W_{18}O_{49}$ NPs (control in Fig. 5C) indicates that the $W_{18}O_{49}$ NPs also possess good photothermal efficiency. Unfortunately, $W_{18}O_{49}$ NPs are difficult to keep stable in water without the isolation of oxygen, and the spectrum of the naked $W_{18}O_{49}$ NPs is notably changed after they are stored for only one week.

From Fig. 5C, it can be seen that the temperature of the $W_{18}O_{49}$ NPs rises as a function of time; however, the photothermal efficiency declines sharply after just 1 week retention. In contrast, from Fig. 5D we can see that the photothermal efficiency of the $W_{18}O_{49}$@PEG-PCL NPs does not change much even after 3 weeks of retention, because the PEG-PCL NPs protect the $W_{18}O_{49}$ NPs from hydrolysis and oxidation in aqueous solution. Finally, the temperature reaches 56.8 °C and 35.3 °C respectively, for the $W_{18}O_{49}$@PEG-PCL NPs (Fig. 5D) and the $W_{18}O_{49}$ NPs (Fig. 5C). Obviously, the $W_{18}O_{49}$@PEG-PCL NPs have the potential for cancer cell killing. In order to further demonstrate the photothermal conversion stability of our NPs, five cycles of NIR laser irradiation (0.5 W cm^{-2}, 1064/808 nm laser, 10 min)/cooling down (1 h) procedure were performed for the $W_{18}O_{49}$@PEG-PCL NPs and Au nanorods (the most common PTT agent), respectively (Fig. 6). From the UV spectra (Fig. 6A and) Fig. 6B), the $W_{18}O_{49}$@PEG-PCL NPs clearly exhibit better photothermal conversion stability, because the $W_{18}O_{49}$ NPs are uniformly spherical and in the most stable conformation, while the Au nanorods are club-shaped. Hyperthermia causes Au nanorods to become out of shape and they can be transformed from club-shaped to spherical-shaped (Fig. 6C). Additionally, from Fig. 6D, we can find that after five cycles, the elevation of the temperature of the $W_{18}O_{49}$@PEG-PCL NPs does not fade much compared to that of the Au nanorods. We selected the fifth full cycle, and the final photothermal conversion efficiency (η) for the $W_{18}O_{49}$@PEG-PCL NPs and the Au nanorods was 65.8% and 16.8%, respectively. All these results show that our NPs can be superior over the Au nanorods.

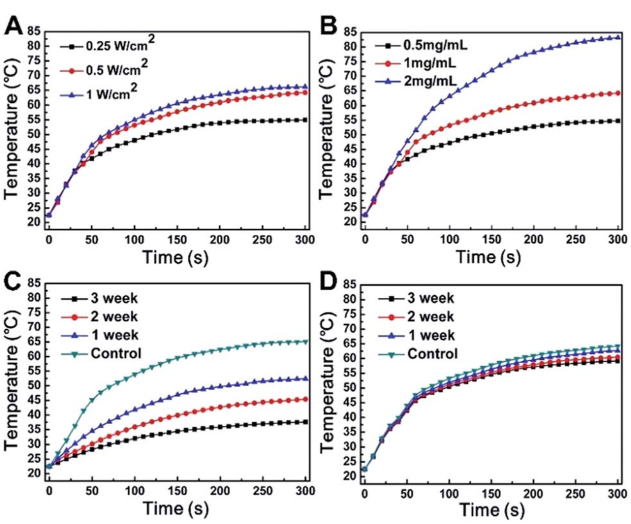

Fig. 5 (A–C) Temperature elevation of aqueous dispersions of $W_{18}O_{49}$@PEG-PCL NPs as a function of time (0–300 seconds) under irradiation with light of wavelength 1064 nm. (A) Different power densities of the 1064 nm laser at the concentration of 1 mg mL^{-1}. (B) Different concentrations under the 0.5 W cm^{-2} 1064 nm laser. (C) Temperature elevation of the $W_{18}O_{49}$ NPs after 1, 2 and 3 weeks of storage in aqueous dispersion, at a concentration of 1 mg mL^{-1} and under a 0.5 W cm^{-2} 1064 nm laser. (D) Temperature elevation of the $W_{18}O_{49}$@PEG-PCL NPs after 1, 2 and 3 weeks of storage in aqueous dispersion, as a function of time (0–300 seconds), at a concentration of 1 mg mL^{-1} and under a 0.5 W cm^{-2} 1064 nm laser.

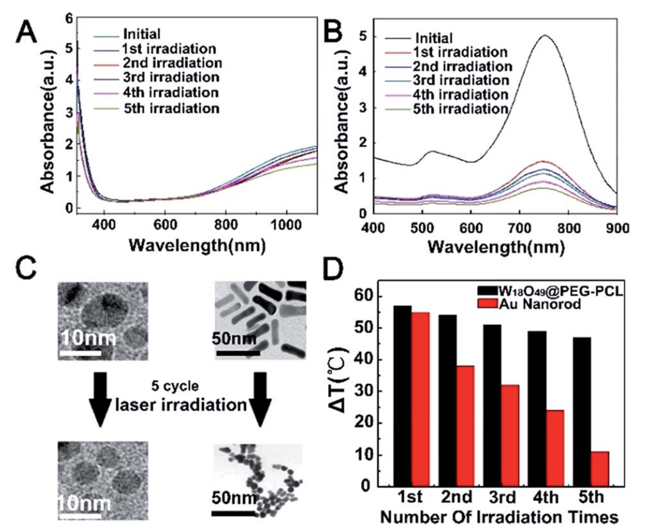

Fig. 6 (A–D) Five cycles of NIR laser irradiation (0.5 W cm^{-2}, 1064/808 nm laser, 10 min)/cooling down (1 h) procedure were performed. (A) UV-vis spectra of $W_{18}O_{49}$@PEG-PCL NPs; (B) UV-vis spectra of Au nanorods; (C) TEM of $W_{18}O_{49}$@PEG-PCL NPs and Au nanorods; (D) elevation of the temperature of $W_{18}O_{49}$@PEG-PCL NPs and Au nanorods.

To explore the cytotoxicity of the $W_{18}O_{49}$@PEG-PCL NPs, the cellular uptake of $W_{18}O_{49}$@PEG-PCL NPs by HeLa cells was examined using a fluorescent microscope (Fig. 7). In Fig. 7, nuclei with blue fluorescence and f-actin with green fluorescence can be clearly seen in the images, indicating the successful staining of the nuclei with DAPI and the f-actin with FITC labeled phalloidine. After 2 h incubation, no red fluorescence was seen in the group containing the $W_{18}O_{49}$ NPs and fewer purple spots were seen in the merged images, which indicated that no, or a very small amount of, $W_{18}O_{49}$ NPs entered into the HeLa cells. However, in the cells treated with $W_{18}O_{49}$@PEG-PCL NPs, red color was observed, indicating the existence of $W_{18}O_{49}$@PEG-PCL NPs, and according to the merged images, purple sports were present, which indicated that $W_{18}O_{49}$@PEG-PCL NPs were internalized by the nuclei, strongly suggesting the remarkable uptake of the $W_{18}O_{49}$@PEG-PCL NPs by the cells. We think that equipping $W_{18}O_{49}$ with PEG-PCL ($W_{18}O_{49}$, 6.7 nm, $W_{18}O_{49}$@PEG-PCL, 108 nm) can take advantage of the enhanced permeability and retention effect (EPR) to implement passive enrichment of the NPs at the tumor location. Positively charged nanoparticles have higher cellular uptake than negatively charged nanoparticles. From the results in Table 2, we can see that the zeta potentials for $W_{18}O_{49}$@PEG-PCL and $W_{18}O_{49}$ were 1.61 ± 0.69 mV and −30.82 ± 1.64 mV, and this is another reason for the fact that the PEG-PCL NPs enhance the internalization of $W_{18}O_{49}$ NPs in cells.

Table 2 The zeta potentials of the $W_{18}O_{49}$ NPs and $W_{18}O_{49}$@PEG-PCL NPs

	Zeta (mV)
$W_{18}O_{49}$	−30.82 ± 1.64
$W_{18}O_{49}$@PEG-PCL	1.61 ± 0.69

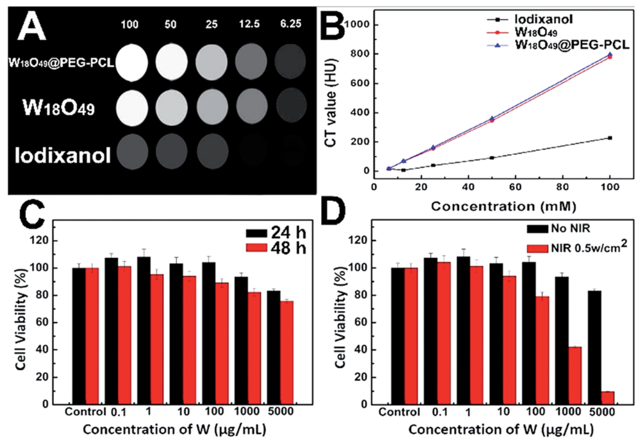

Fig. 8 (A) CT images of the $W_{18}O_{49}$ NPs, $W_{18}O_{49}$@PEG-PCL NPs and iodixanol; (B) *in vitro* X-ray attenuation assay of $W_{18}O_{49}$ NPs, $W_{18}O_{49}$@PEG-PCL NPs and iodixanol respectively; (C) *in vitro* viability of HeLa cells in the presence of $W_{18}O_{49}$@PEG-PCL NPs at different concentrations for 24 and 48 h; (D) *in vitro* viability of HeLa cells incubated with $W_{18}O_{49}$@PEG-PCL NPs at different concentrations for 24 h irradiated with NIR laser or not. The results represent the mean ± SD ($n = 3$).

In vitro CT study and cytotoxic assay

Fig. 8A shows the CT images of the clinically used iodine contrast agent (Iodixanol), $W_{18}O_{49}$ NPs and $W_{18}O_{49}$@PEG-PCL NPs. Clearly, the $W_{18}O_{49}$ NPs and $W_{18}O_{49}$@PEG-PCL NPs show brighter images than iodixanol, which confirms their superior enhanced contrast ability in CT measurements.

Fig. 8B displays the results of the *in vitro* X-ray attenuating assay. The $W_{18}O_{49}$ NPs and $W_{18}O_{49}$@PEG-PCL NPs exhibit a concentration dependent CT enhancement, and their Hounsfield Unit (HU) values are very close, and are much higher than that of iodixanol at the same concentration. Before translation into *in vivo* usage, the biocompatibility of $W_{18}O_{49}$@PEG-PCL NPs was evaluated. The results of the MTT assay indicated that the $W_{18}O_{49}$@PEG-PCL NPs exerted negligible cytotoxic effect on the cell viability within the concentration range of 0.1–5000 μg mL^{-1} after 24 h incubation (Fig. 8C). Even when the concentration of tungsten reached up to 5000 μg mL^{-1} after 48 h incubation, only a slight reduction in cell viability (22.4%) was observed, which reveals that the $W_{18}O_{49}$@PEG-PCL NPs exhibit good biocompatibility and are suitable for *in vivo* applications. The *in vitro* cytotoxicity of the PTT effect arising from the $W_{18}O_{49}$@PEG-PCL NPs was also evaluated by MTT assay. HeLa cells were incubated with $W_{18}O_{49}$@PEG-PCL NPs, and irradiated or not by NIR laser with an energy density of 0.5 W cm^{-2} for 4 min. From Fig. 8D, it can be seen that the $W_{18}O_{49}$@PEG-PCL NPs do not show any cytotoxicity in the case of no irradiation. However, when the cells are subject to NIR irradiation, a dose-dependent cytotoxicity is observed, and the cytotoxicity of the $W_{18}O_{49}$@PEG-PCL NPs is significant at a concentration of 5000 μg mL^{-1}, with only 9.5% of cells surviving after 24 h incubation, illustrating that the PTT effect arising from the $W_{18}O_{49}$@PEG-PCL NPs could be used in cancer therapy at an appropriate concentration.

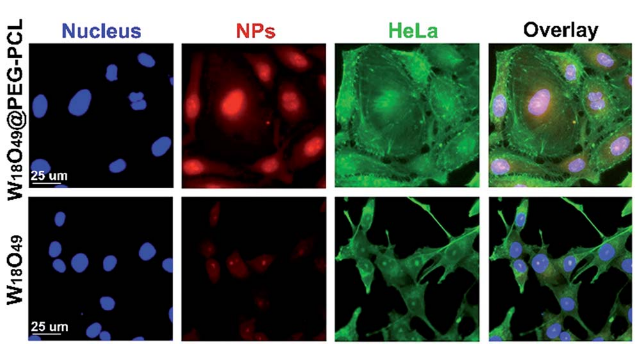

Fig. 7 Fluorescence microscope images of HeLa cells incubated with NPs for 2 h. The cell nuclei and f-actin were stained by DAPI (blue) and FITC labeled phalloidine (green), respectively. NPs were conjugated with Cy5.5 (red).

In vitro PTT capability verified *via* live/dead double staining method

The *in vitro* PTT therapeutic outcome of cells after different treatments was verified *via* a live/dead double staining method

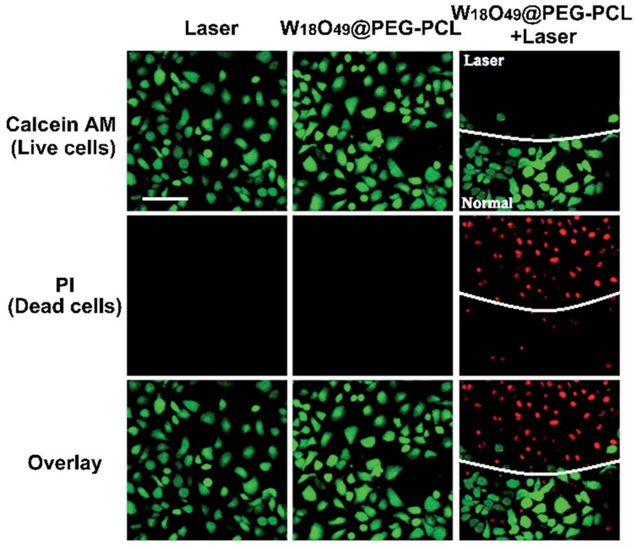

Fig. 9 (From left to right) Cell viability of HeLa cells after undergoing laser treatment, after $W_{18}O_{49}$@PEG-PCL NP incubation without laser irradiation and after $W_{18}O_{49}$@PEG-PCL NP incubation with laser irradiation. Viable and dead cells are highlighted in green and red by calcein AM and PI staining, respectively. Scale bar: 50 μm.

(Fig. 9). Calcein AM can stain live cells with green and PI dye can stain dead cells with red.

No red color was seen from the HeLa cells when they were irradiated by laser irradiation or incubated with $W_{18}O_{49}$@PEG-PCL NPs alone, which indicates that this treatment does not exert any obvious damage to the HeLa cells. However, for cells treated with $W_{18}O_{49}$@PEG-PCL NPs plus laser irradiation, red fluorescence corresponding to dead cells within laser spots was seen, indicating the superior PTT potency of $W_{18}O_{49}$@PEG-PCL NPs against HeLa cells. These results clearly confirm that $W_{18}O_{49}$@PEG-PCL NPs can be used for the treatment of cancer *via* PTT.

Conclusions

In conclusion, we synthesized $W_{18}O_{49}$@PEG-PCL NPs by encapsulating $W_{18}O_{49}$ within PEG-PCL NPs. The PEG-PCL NPs enhance the biocompatibility, stability and internalization of $W_{18}O_{49}$ NPs in cells. These $W_{18}O_{49}$@PEG-PCL NPs exhibit low cytotoxicity, wonderful photothermal effects, excellent CT efficiency and can be retained for a long time, conferring them with the potential to play an active role in future clinical trials. Last but not least, Hwang's research suggests that $W_{18}O_{49}$ NPs can also stimulate Radical Oxygen Species (ROS).[24] Accumulating evidence confirms that the enrichment of tumor promoting cells in hypoxic regions[25] can protect tumor cells from cytolysis induced by chemotherapy or radiotherapy (RT),[26] and contribute to lethal local recurrence rapidly. On this basis, reversing the hypoxic microenvironment is crucial for achieving an optimal therapeutic outcome. We believe that ROS will be achieved in hypoxic regions during the PTT procedure of our $W_{18}O_{49}$@PEG-PCL NPs and this will significantly enhance the susceptibility of hypoxic cancer cells to radiation.

Acknowledgements

This study was funded by the National Natural Science Foundation of China (No. 81172362) and Shaanxi Science & Technology Co-ordination & Innovation Project (2013KTCQ03-08).

Notes and references

1 C. Y. Li, Z. J. Liu and P. Yao, *RSC Adv.*, 2016, **6**, 33083–33091.
2 J. Feng, D. Chang, Z. F. Wang, B. Shen, J. J. Yang, Y. Y. Jiang, S. H. Ju and N. Y. He, *RSC Adv.*, 2014, **4**, 51950–51959.
3 D. Xi, S. Dong, X. X. Meng, Q. H Lu, L. J. Meng and J. Ye, *RSC Adv.*, 2012, **2**, 12515–12524.
4 D. Kim, Y. Y. Jeong and S. Jon, *ACS Nano*, 2010, **4**, 3689–3696.
5 S. W. Chou, Y. H. Shau, P. C. Wu, Y. S. Yang, D. B. Shieh and C. C. Chen, *J. Am. Chem. Soc.*, 2010, **132**, 13270–13278.
6 O. Rabin, J. M. Perez, J. Grimm, G. Wojtkiewicz and R. Weissleder, *Nat. Mater.*, 2006, **5**, 118–122.
7 H. Liu, H. Wang, R. Guo, X. Y. Cao, J. L. Zhao, Y. Luo, M. W. Shen, G. X. Zhang and X. Y. Shi, *Polym. Chem.*, 2010, **1**, 1677–1683.
8 P. J. Bonitatibus, A. S. Torres, B. Kandapallil, B. D. Lee, G. D. Goddard, R. E. Colborn and M. E. Marino, *ACS Nano*, 2012, **6**, 6650–6658.
9 D. Huo, J. He, H. Li, A. J. Huang, H. Y. Zhao, Y. Ding, Z. Y. Zhou and Y. Hu, *Biomaterials*, 2014, **35**, 9155–9166.
10 K. Dong, Z. Liu, J. H. Liu, S. Huang, Z. H. Li, Q. H. Yuan, J. S. Ren and X. G. Qu, *Nanoscale*, 2014, **6**, 2211–2217.
11 Z. Liu, X. J. Liu, X. Ran, E. G. Ju, J. S. Ren and X. G. Qu, *Biomaterials*, 2015, **69**, 56–64.
12 Z. Liu, J. H. Liu, R. Wang, Y. D. Du, J. S. Ren and X. G. Qu, *Biomaterials*, 2015, **56**, 206–218.
13 Z. Liu, Z. H. Li, J. H. Liu, S. Gu, Q. H. Yuan, J. S. Ren and X. G. Qu, *Biomaterials*, 2012, **33**, 6748–6757.
14 Q. Yin, X. Y. Jin, G. C. Yang, C. H. Jiang, Z. K. Song and G. Y. Sun, *RSC Adv.*, 2014, **4**, 53561–53569.
15 P. Zhang, Y. Y. He, J. H. Liu, J. Feng, Z. Q. Sun, P. P. Lei, Q. H. Yuan and H. J. Zhang, *RSC Adv.*, 2016, **6**, 14283–14289.
16 J. H. Liu, J. G. Han, Z. C. Kang, R. Golamaully, N. N. Xu, H. P. Li and X. L. Han, *Nanoscale*, 2014, **6**, 5770–5776.
17 H. Kobayashi, Y. Hama, Y. Koyama, T. Barrett, C. A. S. Regino, Y. Urano and P. L. Choyke, *Nano Lett.*, 2007, **7**, 1711–1716.
18 K. H. Kim and R. G. Geronemus, *Dermatol. Surg.*, 2006, **32**, 241–248.
19 G. L. Wolf, R. L. Arenson and A. P. Cross, *AJR, Am. J. Roentgenol.*, 1989, **152**, 939–944.
20 H. Maeda, K. Tsukigawa and J. Fang, *Microcirculation*, 2016, **23**, 173–182.
21 J. Fang, L. Long and H. Maeda, *Methods Mol. Biol.*, 2016, **1409**, 9–23.

22 H. Maeda, *Adv. Drug Delivery Rev.*, 2015, **91**, 3–6.
23 Z. G. Zhou, B. Kong, C. Yu, X. Y. Shi, M. W. Wang, W. Liu, Y. N. Sun, Y. J. Zhang, H. Yang and S. P. Yang, *Sci. Rep.*, 2014, **4**, 3653–3663.
24 Z. G. Chen, Q. Wang, H. L. Wang, L. S. Zhang, G. S. Song, L. L. Song, J. Q. Hu, H. Z. Wang, J. S. Liu, M. F. Zhu and D. Y. Zhao, *Adv. Mater.*, 2013, **25**, 2095–2100.
25 M. L. Song, T. Liu, C. R. Shi, X. Z. Zhang and X. Y. Chen, *ACS Nano*, 2016, **10**, 633–647.
26 B. A. Teicher, *Cancer Metastasis Rev.*, 1994, **13**, 139–168.
27 C. S. Guo, S. Yin, Q. Dong and T. Sato, *RSC Adv.*, 2012, **2**, 5041–5043.